

Mechanical properties and microstructure of magnesium alloy Mg₂₂Gd processed by severe plastic deformation

Miloš Janeček^{1*}, Peter Minárik¹, Tomáš Krajnák¹, Kristína Václavová¹, Josef Stráský¹, Jakub Čížek², Marian Vlček², Jozef Veselý¹, Jung Gi Kim³, Hyoung Seop Kim³

¹Department of Physics of Materials, Charles University, Ke Karlovu 5, Prague 2, 12116, Czech Republic

²Department of Low Temperature Physics, Charles University, V Holešovičkách 747, Prague 8, 18000, Czech Republic

³Department of Materials Science and Engineering, Pohang University of Science and Technology, Pohang 790-784, South Korea

*Corresponding author: Tel: (+420) 951551358, E-mail: janecek@met.mff.cuni.cz

Received: 29 December 2016, Revised: 12 January 2017 and Accepted: 09 April 2017

DOI: 10.5185/amlett.2017.1582

www.vbripress.com/aml

Abstract

Mg₂₂Gd alloy was processed by high pressure torsion (HPT) at room temperature and the pressure of 2 GPa. A series of specimens with different number of rotations N ($N = 0-15$) was prepared from the initial coarse grained as-cast material. Mechanical properties were investigated by microhardness mapping. The microhardness was found to increase with increasing strain imposed by HPT and tend to saturate at about $HV = 145$. The microstructure (phase morphology and composition, etc.) evolution with strain was investigated by scanning electron microscopy and EDS. High Gd content in the alloy resulted in the precipitation of stable Mg₅Gd phase. This phase exhibited apparently higher hardness than the magnesium matrix. During straining the phase was continuously fragmented and only tiny particles were found in heavily strained material. Electron back scatter diffraction (EBSD) and automated crystallographic orientation mapping in transmission electron microscope (ACOM-TEM) were employed to characterize the fragmentation of the grain structure. HPT was found to result in strong grain refinement by the factor of approximately 1000. The dislocation density was determined by positron annihilation spectroscopy. Significant twinning was found in the initial stages of HPT straining. At high strains twin formation was suppressed and only dislocation storage in the material occurs. Copyright © 2017 VBRI Press.

Keywords: High pressure torsion, MgGd alloy, electron microscopy, microstructure, microhardness.

Introduction

Magnesium alloys are known as lightweight metallic materials with high specific strength. High strength values were achieved in binary Mg-Gd alloys [1-3] and more complicated ternary and quaternary alloys [4-6]. Gd as an alloying element provides some solid solution strengthening [7], although its solubility limit at room temperature is very low [8]. Further strengthening is provided by precipitation sequence resulting in the formation of metastable β' and stable Mg₅Gd particles [9,10]. Additional strengthening can be achieved by complementary mechanism of grain refinement. Apart from increased strength, the ultra-fine grained (UFG) microstructure enhances possible superplastic properties at elevated temperatures. On the other hand, superplastic behavior is limited by the thermal stability of UFG microstructure [11,12]. Alloying by Gd suppresses continuous recrystallization (grain growth) via pinning of

grain boundaries [13] and therefore enhances the superplasticity [14-16]. The positive effect of alloying by Gd is therefore threefold and can be summarized as: a) Gd provides solid solution strengthening, b) Gd provides precipitation strengthening and c) Gd enhances superplastic properties via increased thermal stability of the UFG microstructure.

The content of alloying elements in most of the developed binary Mg-Gd alloys and similar ternary and quaternary alloys is limited to few weight percent. Therefore, the alloying elements can fully dissolve in Mg-matrix at elevated temperatures (usually at around 530°C) [7]. Subsequent thermal treatment aims on precipitation of finely dispersed particles to maximize the effect of precipitation strengthening [6]. In this study Mg₂₂Gd (wt.%) alloy was used, where the Gd content is close to the solubility limit at 540-550°C [8]. An alternative approach to disperse precipitates of other phase is employing severe plastic deformation techniques.

Ultrafine grained Mg alloys can be prepared by well-known methods of severe plastic deformation (SPD) such as equal channel angular pressing (ECAP) or high-pressure torsion (HPT) [17,18]. In this study Mg22Gd alloy was prepared by HPT. Detailed study on microstructural changes caused by severe plastic deformation is necessary before evaluating the microstructural stability and superplastic properties [15].

HPT affects the material microstructure in several ways. First, it introduces the high density of dislocations that subsequently form dislocation walls, sub-grain boundaries and finally high angle grain boundaries [19]. Second, plastic deformation in Mg alloys causes twinning [20], which may also contribute to microstructural refinement [21]. Finally, precipitates of the secondary phase might be deformed and fragmented by intensive plastic deformation [22].

Wide palette of experimental techniques was utilized to characterize these complex microstructural changes in Mg22Gd alloy. Experimental techniques include scanning electron microscopy (SEM), electron back-scattered diffraction (EBSD), transmission electron microscopy (TEM), automated crystal orientation microscopy (ACOM-TEM) and positron annihilation spectroscopy (PAS).

Experimental

Specimen preparation

Mg-22 wt.% Gd alloy was processed by squeeze casting in the combined protective environment of Ar and SF₆. After casting, the material was annealed for 5 hours at 530°C followed by a water quench. The overall concentration of Gd as determined by chemical analysis was 22.4±0.4 wt.%. Subsequently, specimens were processed by HPT. The schematic of the HPT device is described in detail elsewhere [23]. It consists of two massive anvils. The specimen in the form of a tiny disk is placed between the anvils. The processing is divided into two steps. In the first step (compression stage), both anvils are pressed together, while in the second step (torsional stage) one of the anvils begins to turn imposing pure torsional straining to the disk specimen. The equivalent von Mises strain e_{equiv} which is imposed to the specimen during straining is expressed by the following relation [24]:

$$e_{equiv} = \frac{1}{\sqrt{3}} \frac{2\pi r N}{h}, \quad (1)$$

where, r is the distance from the disk centre which lies in the rotation axis, N is the number of HPT turns and h is the specimen thickness. It is obvious that the HPT straining introduces a lateral inhomogeneity to the disk where the imposed strain increases with increasing distance from the specimen centre. As a consequence, the inhomogeneous microstructure may be expected. Due to this reason, we divided the surface of individual disks into three regions which will be referred to in the text as follows: centre - $r = 0-0.5$ mm, middle - $r = 3-5$ mm and

periphery - $r=7-9$ mm. In order to investigate the microstructure evolution and the development of mechanical properties a series of specimens having the diameter of 10 mm and the approximate thickness of 1 mm with different number of HPT turns N was prepared, namely $N = 1/4, 1/2, 1, 3, 5, 10, 15$. As an initial condition the specimen which was only pressed with no further torsion was also prepared – hereinafter referred to as $N = 0$ only. HPT processing was done at room temperature and by applying the pressure of 2 GPa. The rotation speed was 1 rpm.

Characterization of the microstructure

High resolution scanning electron microscope Zeiss Auriga Cross Beam™ FEG/FIB equipped with EDX and EBSD was used for the microstructure characterization. Detail observations of microstructure and lattice defects were performed on the transmission electron microscope Jeol 2000FX operated at 200 kV. Initial stages of grain fragmentation and twinning were obtained from EBSD analysis. However, the ultrafine-grained character of the microstructure in specimens with higher imposed strains (for the higher number of turns and/or in peripheral regions of the disks) disallowed to perform standard EBSD scans on SEM due to its limited resolution. In this case a special technique called ACOM-TEM (Automated Crystallographic Orientation Mapping in TEM) was employed. Unlike EBSD which uses Kikuchi lines for the orientation determination, in ACOM-TEM the orientation is determined from the point diffraction pattern obtained in TEM using beam precession. Due to much higher lateral resolution of TEM, the orientation map is obtained with much higher resolution (step size 5 nm, acceleration voltage – 200 kV and 50 fps - the data acquisition speed in our case). The details of this technique may be found elsewhere [25]. High resolution TEM/STEM JEOL JEM 2200FS with precession diffraction Nanos was employed for this special measurement. The only disadvantage of this technique is its local character, therefore more scans in different zones must be performed to check for any microstructural inhomogeneities.

Microhardness measurement

Variations of mechanical properties with strain imposed by HPT were assessed by Vickers microhardness measurement. An automatic microhardness tester Qness™ Q10 was employed. A quite dense mesh of measuring points consisting of concentric circles including more than 1000 indents was used to characterize in detail microhardness variations throughout the surface of individual HPT disks.

Measurement of dislocation density

It is well known that specimens deformed by severe plastic deformation contain a high density of dislocations and other lattice defects. Positron annihilation spectroscopy was employed to determine the dislocation density in individual specimens. In this technique a source of positrons (²²Na with the activity of 1.5 MBq) is sealed between two identical specimens. The ²²Na radioisotope

decays into ^{22}Ne and emits high energy positrons (the mean energy ~ 250 keV). The daughter ^{22}Ne nucleus is in an excited state and de-excites by emission of gamma ray with the energy of 1274 keV. This so-called start photon that is detected by a scintillation detector is emitted virtually simultaneously with the positron and provides information when the positron was born. Positrons penetrating into the specimen are quickly thermalized, i.e. they lose their energy down to the thermal energy ($kT \sim 0.03$ eV). They diffuse in the lattice and when they meet an electron they annihilate. The annihilation process is accompanied by the emission of annihilation gamma rays that are detected by a scintillation detector. The time difference between the start and the annihilation gamma ray determines the lifetime of an individual positron. In a perfect crystal lattice positrons are in the delocalized state – so called free positrons. Due to the presence of open volume defects some positrons are trapped in these regions and live longer than free ones. The details of this technique may be found elsewhere [26, 27].

The measured spectrum consists of exponential decay components convoluted with resolution function of the spectrometer. Each component corresponds to a certain positron state. In heavily deformed specimens, as in our case, the spectrum consists of a free positron component with shorter lifetime and a longer component that comes from positrons trapped at dislocations. The lifetime of positrons trapped at dislocations in Mg is $\tau_d \sim 250$ ps [1]. This lifetime is constant disregarding the dislocation density. On the other hand, the lifetime τ_f of the free positron component decreases with increasing dislocation density, since trapping at dislocations is additional channel that decreases the population of free positrons in addition to their annihilation in the free state. The mean lifetime is given by the following equation:

$$\tau_{mean} = I_f \tau_f + I_d \tau_d, \quad (2)$$

where, I_f and I_d are intensities of components associated with free positron and dislocation component, respectively. Increasing values of τ_{mean} correlate with increasing dislocation density. Hence, τ_{mean} can be considered as a certain measure of dislocation density in the sample.

Results and discussion

SEM observations

The detail of the microstructure of the alloy in the as pressed condition ($N=0$) is shown in **Fig. 1(a)**. It is clear that the annealing at 530°C for 5 h did not lead to complete dissolution of Gd in the matrix. Marked with the green arrow are particles of equilibrium phase Mg_5Gd which were found to be randomly distributed in the α -matrix (solid solution of Gd in Mg). The chemical composition of these particles was confirmed by EDX analysis and is shown in **Fig. 1(b)** – green curve. Next to Mg_5Gd particles, numerous isolated tiny rectangular particles were found in the material. One example of such particle is marked with a blue arrow in **Fig. 1(a)**. The bright character of the Z-contrast indicates the enhanced content of Gd in these particles when compared to Mg_5Gd . Furthermore, the EDX analysis did not reveal the presence of any other element than Gd in these particles (see the blue curve in **Fig. 1(b)**). Some authors designate similarly looking particles as Mg_5Gd [8] or Mg_3Gd [4], while in [28] it is claimed that such particles are “rich in Gd”, which is consistent with our findings. In [29] it is reported that these particles in MgGd alloys belong to gadolinium di-hydride (GdH_2) phase. Hydrogen as a light element cannot be obviously detected by EDX technique. In a recent publication [30] it is shown that these particles are indeed GdH_2 . According to the authors of Ref. [30], GdH_2 particles are formed during the preparation of the

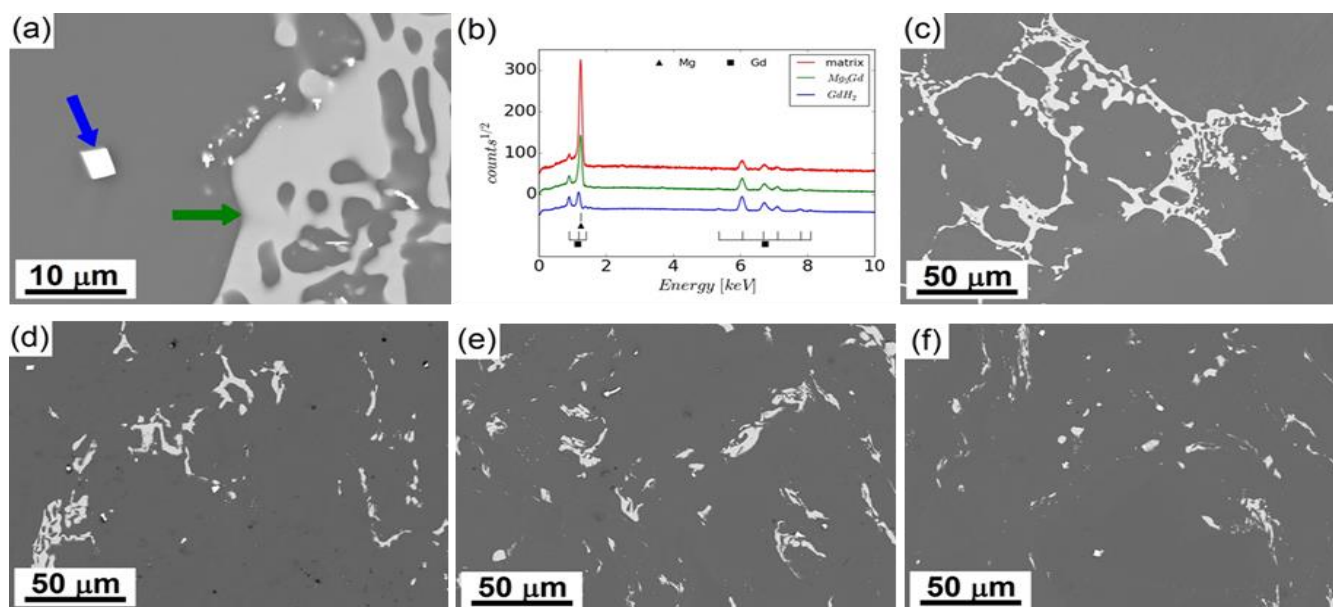


Fig. 1. SEM micrographs of the phase structure and its fragmentation resulting from HPT straining (BSE, Z-contrast) (a) $N = 0$ detail, (b) EDX spectrum, (c) $N = 0$, (d) $N = 1$, (e) $N = 5$, (f) $N = 15$.

specimen in aqueous environment due to high affinity of Gd and H. **Fig. 1(c-f)** shows the influence of severe plastic deformation on the morphology of Mg_5Gd particles. The SEM micrographs were taken from the middle regions of individual HPT disks ($r = 0-0.5$ mm). The gradual decomposition and fragmentation of the Mg_5Gd phase particles is clearly seen. Already after a single HPT turn the phase loses its compactness which continues with further straining. In the specimen, $N = 15$ small precipitates randomly dispersed in the matrix may be observed, see **Fig. 1(f)**. High strains imposed by HPT therefore completely disintegrate the phases in the alloy.

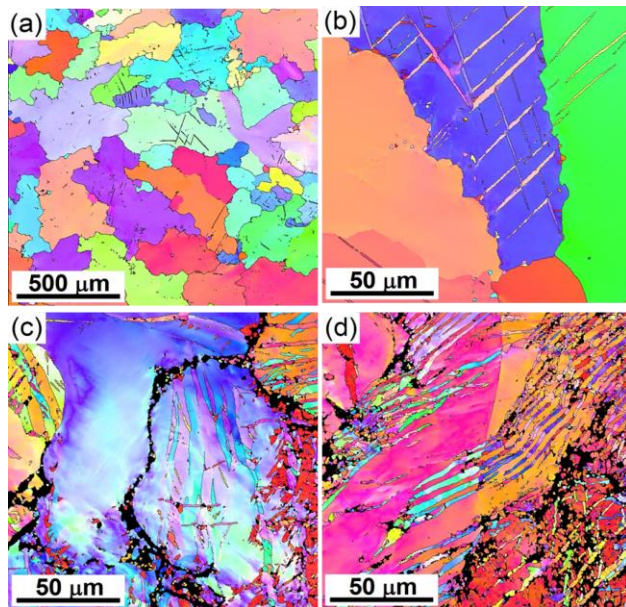


Fig. 2. EBSD IPF images of microstructure evolution in initial stages of HPT straining (a) $N = 0$, centre, (b) $N = 0$, centre - twinned grain, (c) $N = 1/2$, centre, (d) $N = 1/2$, middle part.

EBSD and ACOM-TEM investigation

Fig. 2. shows EBSD IPF maps of the microstructure of the alloy. The microstructure of the as pressed material $N = 0$ (**Fig. 2(a)**) consists of almost equiaxed grains of the average size of about 300-350 μm (fully comparable to the as-cast material). The compressing stage of HPT did not cause any apparent grain refinement, while some twins were formed in several grains which were suitably oriented for twinning. An example of such a grain is shown in **Fig. 2(b)**, where two families of twins are clearly seen. Torsional straining by HPT significantly influences the microstructure evolution. Similarly as in other magnesium alloys the grain fragmentation is inhomogeneous [31,32] and results in the formation of the bimodal structure [18]. In **Fig. 2(c)** the detail of the microstructure of the central part of the specimen subjected to a half of a turn ($N = 1/2$) is shown. Apparent formation of UFG grains around the central nonfragmented grain is clearly seen at the EBSD map. Moreover, extensive twinning occurs in several grains. The intensity of twinning increases significantly with increasing strain. In the middle part of the specimen

$N = 1/2$, in **Fig. 2(d)** the twins are found almost in all grains. Some of them extend through several grains and form wide twin bands. A detail inspection of EBSD map indicates that orientation of twin facets changes in individual grains and results in grain disintegration and fragmentation. At these relatively low strains twinning becomes the controlling mechanism of grain fragmentation and the overall structure fragmentation [21]. Starting with the specimen $N = 1$ the high imposed strain and consequent storage of the high density of dislocations and the presence of high stresses in individual grains disallowed to determine the orientation from EBSD. ACOM-TEM is a useful technique providing sufficient resolution for the determination of the orientation in heavily deformed, ultrafine-grained structures. **Fig. 3.** shows ACOM-TEM images of the microstructure evolution in specimens $N \geq 1$. All images were obtained from peripheral parts of the specimens, where the maximum grain refinement is expected. The continuous grain refinement with increasing number of turns is clearly seen. In the specimen $N = 1$ a heavily bent coarse grain of the approximate size of 1 μm is surrounded by several small nanocrystalline grains.

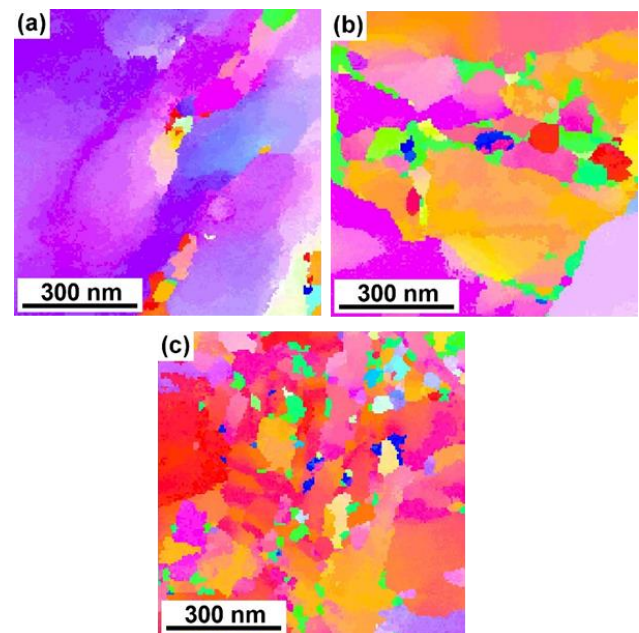


Fig. 3. ACOM-TEM orientation maps acquired from samples of $Mg_{22}Gd$ alloy subjected to various number of HPT turns N : (a) $N = 1$; (b) $N = 5$ and (c) $N = 15$.

Apparently smaller grain structure with higher fraction of nanocrystalline grains was observed in specimen $N = 5$ as compared to the specimen $N = 1$, cf. **Fig. 3(a)** and **3(b)**. No twins were found in this specimen. The same trend of grain refinement continues up to 15 turns. The microstructure of the specimen is shown in **Fig. 3(c)**. In all three specimens, the distribution of grain sizes is bimodal and two regions are present in the samples. The first region consists of coarser grains, while the second one exhibits UFG or even nanocrystalline structure. It is evident from **Fig. 3** that the disparity of grain sizes is the

largest in the sample subjected to 1 HPT revolution. The difference between these two regions decreases with increasing number of HPT turns. Although the microstructure becomes quite homogeneous after 15 revolutions, the bimodal grain size distribution can be still partly seen in **Fig. 3(c)** indicating that even after 15 turns the complete grain refinement was not achieved, even if the average grains size ranges between 150-200 nm confirming the efficiency of grain refinement by HPT.

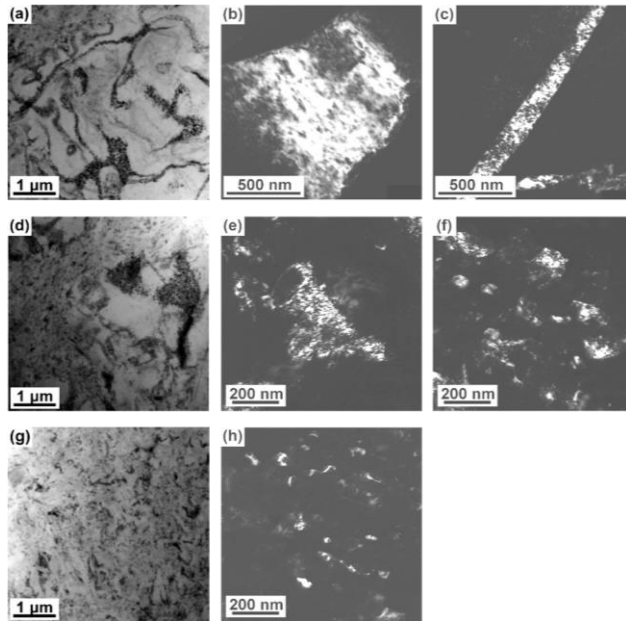


Fig. 4. TEM micrographs showing the evolution of grain structure in Mg22Gd subjected to different number of HPT turns : (a) BF - $N = 1$; (b) DF - $N = 1$ deformed region; (c) DF - twin, $N = 1$, (d) BF - $N = 5$; (e) DF - area with ~ 200 nm grains, $N = 5$; (f) DF - grains smaller than 200 nm, $N = 5$; (g) BF - $N = 15$; (h) DF - grains significantly smaller than 200 nm, $N = 15$.

TEM

The microstructure of samples after 1, 5 and 15 HPT was also examined by transmission electron microscopy. All TEM measurements were performed at the peripheral parts of HPT disks in order to allow a direct comparison with ACOM-TEM IPF maps. TEM micrographs are shown in **Fig. 4**. The specimen after 1 HPT turn ($N = 1$) predominantly consists of heavily deformed micrometer-sized grains as seen in **Fig. 4(a)** and in dark field image in **Fig. 4(b)**. The high internal strain in these grains is demonstrated by the presence of bend contours. Occasionally, twins can be found in the sample after $N = 1$ as seen in **Fig. 4(c)**, while no twins were observed in more deformed conditions. Similarly, very few twins were found during numerous ACOM-TEM scans. This indicates the abrupt change of the controlling mechanism of grain fragmentation from twinning to dislocation storage and rearrangements. Once the strain exceeds a certain value the conditions for twinning become unfavourable and further microstructure refinement is controlled by dislocations. Higher strain conditions are also characterized by smaller grains, which are less prone

to twinning. Areas consisting of refined ultra-fine grains were already observed in the specimen after 1 HPT turn, see the top left corner of **Fig. 4(a)**. However, they were observed only in a small volume fraction of the sample. Relative volume fraction of UFG structure increases with increasing number of HPT turns. In the specimen after 5 turns ($N = 5$), the microstructure is composed of both coarse grains and UFG bands in comparable fractions, see **Fig. 4(d)**, where coarse grain in the right part of the micrograph is surrounded by UFG band from the left and top sides. Dark field TEM images presented in **Figs. 4(e-f)** reveal that there are two regions with different grain sizes within UFG bands in the sample $N = 5$. The first one exhibits the average grain size around 200 nm, see **Fig. 4(e)**, while the second one is composed of significantly smaller grains, see **Fig. 4(f)**. On the other hand, bright-field TEM image of sample subjected to 15 HPT turns shown in **Fig. 4(g)** indicates that almost the whole volume of the sample is transformed into UFG structure after 15 turns. After 15 HPT turns, the grain refinement is even higher and grains having the size well below 200 nm were observed, see **Fig. 4(h)**. The results obtained by TEM and ACOM-TEM are fully consistent. Both methods indicate that the grain refinement continues up to 15 HPT turns where almost the whole volume of the samples contains the UFG structure and coarse micrometer sized grains present in samples subjected to 1 and 5 turns are finally disintegrated.

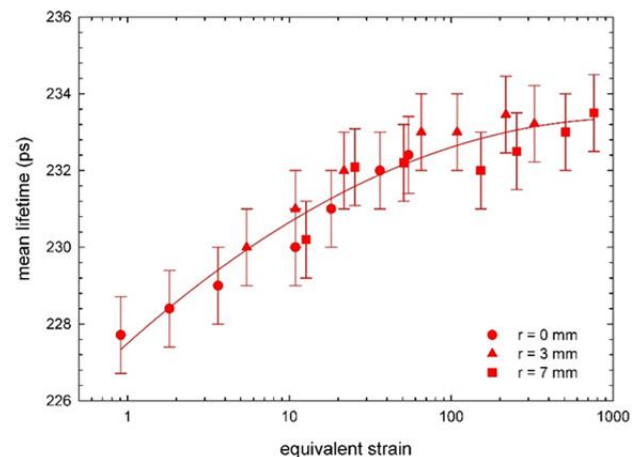


Fig. 5. The dependence of the positron mean life-time as a function of the equivalent strain.

Dislocation density

It is well known that severe plastic deformation introduces in the material a high density of lattice defects which influence the processes of grain refinement. The most important lattice defects stored in the severely plastically deformed material are dislocations. Therefore, the knowledge of the density of dislocations and mainly its evolution with strain provides a valuable microstructure characteristic. Due to the inhomogeneous character of the microstructure in HPT specimens it is common to determine the average value of dislocation density. Positron annihilation spectroscopy (PAS)

measurements were performed in individual specimens subjected to different number of turns. In each specimen three measurements were done, namely in the centre ($r = 0$), in the middle part ($r = 3$ mm) and near the periphery ($r = 7$ mm). The results of PAS measurements are presented in **Fig. 5**, where the master curve of the mean lifetime (τ_{mean}) as a function of the equivalent strain calculated from Eq. (1) is shown. The lifetime of free positrons in a perfect Mg lattice is approximately 225 ps while that of positrons trapped at dislocation in Mg is ~ 250 ps [1,17]. The results of PAS measurement shown in **Fig. 5** indicate that at lower strains the dislocation density is very low ($\tau_{mean} \approx \tau_f$), see Eq. (2). With increasing strain the dislocation density monotonously increases and tends to saturate for very high strains ($\tau_{mean} \approx \tau_d$).

plotted in **Fig. 6**. Due to the inhomogeneous character of the microstructure and the presence of Mg_5Gd and GdH_2 phases, each point depicted in the graph was calculated as an average of all measurements performed at the same distance from the center of the sample disk. As a result, the development of the average HV with the distance from the center r is displayed in **Fig. 6(a)** (so called HV line profiles). Evolution of microhardness exhibits the lateral inhomogeneity of the microstructure with an apparent minimum in the region near the centre and increasing values towards the disk periphery. Samples subjected to torsion straining ($N > 0$) exhibit remarkably higher HV compared to the sample that was only compressed ($N = 0$). The increase of HV is caused by increasing strain which rises both with the distance from the center r and the number of HPT rotations N , see Eq. (1). HV becomes saturated already for $N > 5$, which suggests that the microhardness is affected more by increased dislocation density and initial stages of refinement (including twinning) rather than by the development of fully UFG structure. In order to demonstrate the strengthening effect of HPT on mechanical properties the average value of HV was calculated from all measurements in the individual disks.

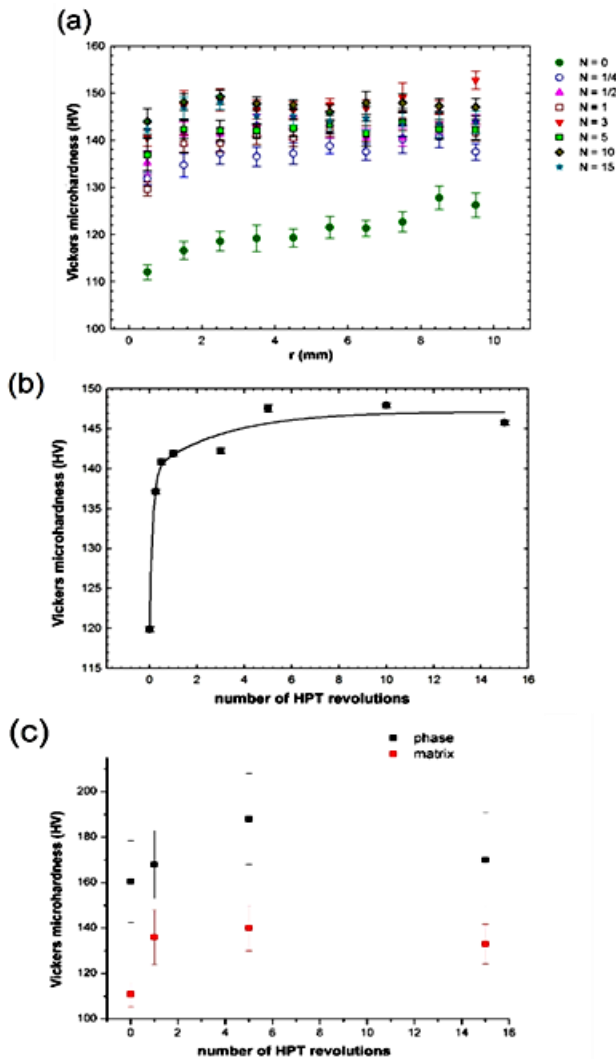


Fig. 6. Vickers microhardness evolution in $Mg_{22}Gd$ subjected to different number of HPT turns (a) line-profiles; (b) average microhardness; (c) microhardness of the matrix and Mg_5Gd phase.

Microhardness

The development of Vickers microhardness (HV 0.1) in samples subjected to various numbers of HPT turns is

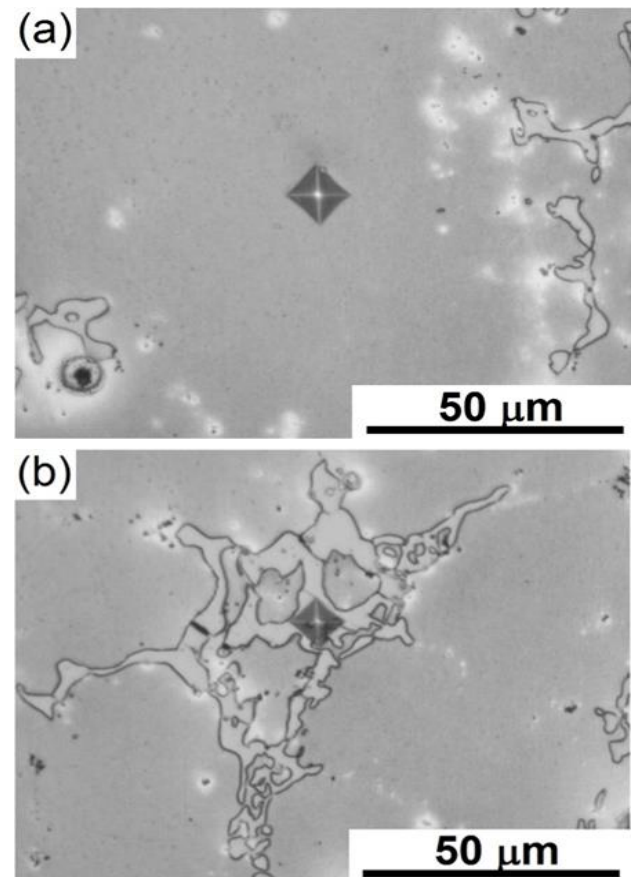


Fig. 7. HV indent positioning for off/on phase HV determination (a) indent in the matrix, (b) indent in Mg_5Gd phase.

This dependence is plotted in **Fig. 6(b)** and indicates clearly the strong strengthening in the initial stages of straining ($N \leq 1$) and the tendency to saturation for higher number of turns ($N > 5$) at the value of $HV \approx 145$. Note

that, the HV of the solution treated material was 105 ± 2 , which is much higher than that of common commercial AZ31 Mg alloy ($HV \sim 60$) and also that the saturated HV of MgGd is higher by 25% than the microhardness of the AZ31 alloy processed by HPT (saturates at around $HV \sim 115$) [18]. However, such measurement did not reveal whether this significant difference in hardness is caused by solid solution strengthening by Gd or Mg₅Gd precipitates. In order to resolve this issue, precise microhardness measurement was used to characterize the differences between the matrix and Mg₅Gd phase in individual specimens. Approximately 50 indents using small loads of 10 gf (HV 0.01) were carefully positioned in the matrix (off phases) and another 50 in the phase. Representative indents positioning is shown schematically in Fig. 7. The results of these measurements are plotted in Fig. 6(c). The microhardness of the Mg₅Gd phase is superior to the microhardness of the matrix irrespective of the specimen. While the matrix HV increases during the initial deformation ($N < 1$) followed by the saturation, the HV of the phase is constant within the measurement uncertainty. The results of HV 0.1 measurement depicted in Fig. 6(b) fit well between the HV of the matrix and of the phase, as could be expected. However, from the values of HV of the matrix it can be seen that the achieved microhardness in Mg₂₂Gd alloy is much higher than that of AZ31 even when the influence of Mg₅Gd precipitates is omitted. It can be therefore concluded that Gd provides significant solid solution hardening even in highly deformed UFG conditions.

Conclusions

The microstructure and microhardness evolution in Mg₂₂Gd alloy subjected to severe plastic deformation by HPT were investigated.

The following conclusions may be drawn from this study:

- Large Mg₅Gd and GdH₂ particles were found in the solution treated alloy. These particles were continuously disintegrated by severe plastic deformation.
- HPT straining introduces the lateral inhomogeneity in the material which is manifested by inhomogeneous dislocation density and grain size throughout the radius of the disk.
- Massive twinning was observed in the initial stages of straining, and the twinning contributes to grain fragmentation. With increasing strain and decreasing grain size, the twinning is suppressed and further grain fragmentation is controlled by rearrangements of stored dislocations.
- Bimodal distribution of grain sizes is formed after twinning is suppressed and the bimodality is continuously smeared out with increased strain due to fragmentation of all grains. Almost homogeneous ultrafine-grained structure was observed in the specimen after 15 HPT rotations.
- Mechanical properties were characterized by Vickers microhardness. Microhardness evolution is consistent

with increased dislocation density and microstructure refinement.

- Microhardness saturates for $N > 5$ of HPT turns.
- Microhardness of Mg₅Gd precipitates is significantly higher than that of the matrix. However, even the microhardness of the matrix (the solid solution of Gd in Mg) after HPT deformation significantly exceeds the microhardness of AZ31 alloy in comparable microstructural condition. This proves that Gd dissolved in Mg matrix provides significant solution strengthening.

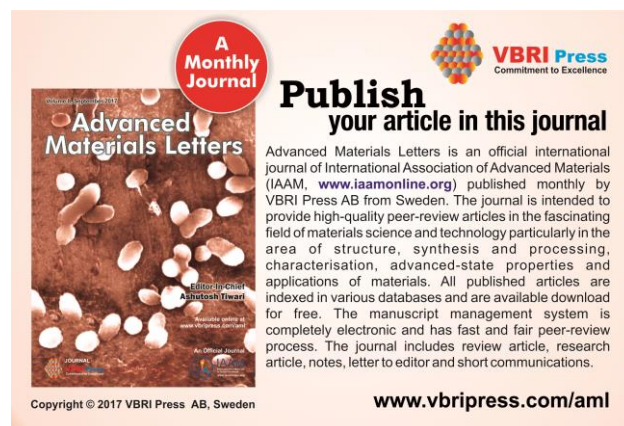
Acknowledgements

This work was financially supported by the Czech Science Foundation (CSF) project no. GB14-36566G. J.C. acknowledges financial support by the CSF project no. 16-12828S. HSK was supported by the Future Material Discovery Project of the National Research Foundation of Korea (NRF) funded by the Ministry of Science, ICT and Future Planning (MSIP) of Korea (NRF-2016M3D1A1023383).

References

1. Čížek, J.; Procházka, I.; Smola, B.; Stulíková, I.; Očenášek, V.; *J. Alloys Compd.*, **2007**, *430*, 92.
DOI: [10.1016/j.jallcom.2006.03.097](https://doi.org/10.1016/j.jallcom.2006.03.097)
2. Kubásek, J.; Vojtěch, D.; *Trans. Nonferrous Met. Soc. China*, **2013**, *23*, 1215.
DOI: [10.1016/S1003-6326\(13\)62586-8](https://doi.org/10.1016/S1003-6326(13)62586-8)
3. Kim, S.H.; Jung, J.G.; You, B.S.; Park, S.H.; *J. Alloys Compd.*, **2017**, *695*, 344.
DOI: [10.1016/j.jallcom.2016.10.179](https://doi.org/10.1016/j.jallcom.2016.10.179)
4. Alizadeh, R.; Mahmudi, R.; Ngan, A. H. W.; Langdon, T. G.; *J. Mater. Sci.*, **2015**, *50*, 4940.
DOI: [10.1007/s10853-015-9041-x](https://doi.org/10.1007/s10853-015-9041-x)
5. Gao, X.; He, S.M.; Zeng, X.Q.; Peng, L.M.; Ding, W.J.; Nie, J.F.; *Mater. Sci. Eng., A*, **2006**, *431*, 322.
DOI: [10.1016/j.msea.2006.06.018](https://doi.org/10.1016/j.msea.2006.06.018)
6. Liu, N.; Zhang, Z.; Peng, L.; Ding, W.; *Mater. Sci. Eng., A*, **2015**, *627*, 223.
DOI: [10.1016/j.msea.2014.12.114](https://doi.org/10.1016/j.msea.2014.12.114)
7. Gao, L.; Chen, R.S.; Han, E.H.; *J. Alloys Compd.*, **2000**, *481*, 379.
DOI: [10.1016/j.jallcom.2009.02.131](https://doi.org/10.1016/j.jallcom.2009.02.131)
8. Peng, Q.; Ma, N.; Li, H.; *J. rare earth*, **2012**, *30*, 1064.
DOI: [10.1016/S1002-0721\(12\)60179-3](https://doi.org/10.1016/S1002-0721(12)60179-3)
9. Čížek, J.; Procházka, I.; Smola, B.; Stulíková, I.; Kužel, R.; Matěj, Z.; Cherkaska, V.; Islamgaliev, R.K.; Kulyasova, O.; *Mater. Sci. Eng., A*, **2007**, *462*, 121.
DOI: [10.1016/j.msea.2006.01.177](https://doi.org/10.1016/j.msea.2006.01.177)
10. Gröbner, J.; Kozlov, A.; Fang, X.Y.; Zhu, S.; Nie, J.F.; Gibson, M.A.; Schmid-Fetzer, R.; *Acta Mater.*, **2015**, *90*, 400.
DOI: [10.1016/j.actamat.2015.02.044](https://doi.org/10.1016/j.actamat.2015.02.044)
11. Stráská, J.; Janeček, M.; Čížek, J.; Stráský, J.; Hadzima, B.; *Mater. Charact.*, **2014**, *94*, 69.
DOI: [10.1016/j.matchar.2014.05.013](https://doi.org/10.1016/j.matchar.2014.05.013)
12. Stráská, J.; Stráský, J.; Minárik, P.; Janeček, M.; Hadzima, B.; *Mater. Sci. Eng., A*, **2017**, *684*, 110.
DOI: [10.1016/j.msea.2016.12.027](https://doi.org/10.1016/j.msea.2016.12.027)
13. Li L.; Zhang, X.; Deng, Y.; Tang, Ch.; *J. Alloys Compd.*, **2009**, *485*, 295.
DOI: [10.1016/j.jallcom.2009.06.113](https://doi.org/10.1016/j.jallcom.2009.06.113)
14. Alizadeh, R.; Mahmudi, R.; Langdon, T.G.; *J. Mater. Res. Technol.*, **2014**, *3*, 228.
DOI: [10.1016/j.jmrt.2014.04.004](https://doi.org/10.1016/j.jmrt.2014.04.004)
15. Alizadeh, R.; Mahmudi, R.; Pereira, P.H.R.; Huang, Y.; Langdon, T.G.; *Mater. Sci. Eng., A*, **2017**, *682*, 577.
DOI: [10.1016/j.msea.2016.11.080](https://doi.org/10.1016/j.msea.2016.11.080)
16. Sarebanzadeh, M.; Roumina, R.; Mahmudi, R.; Wu, G.H.; Jafari Nodoshan, H.R.; *Mater. Sci. Eng., A*, **2015**, *646*, 249.
DOI: [10.1016/j.msea.2015.08.074](https://doi.org/10.1016/j.msea.2015.08.074)

17. Minárik, P.; Král, R.; Čížek, J.; Chmelík, F.; *Acta Mater.*, **2016**, *107*, 83.
DOI: [10.1016/j.actamat.2015.12.050](https://doi.org/10.1016/j.actamat.2015.12.050)
18. Stráská, J.; Janeček, M.; Gubicza, J.; Krajňák, T.; Yoon, E.Y.; Kim, H.S.; *Mater. Sci. Eng., A*, **2015**, *625*, 98.
DOI: [10.1016/j.msea.2014.12.005](https://doi.org/10.1016/j.msea.2014.12.005)
19. Langdon, T.G.; *Acta Mater.*, **2013**, *61*, 7035.
DOI: [10.1016/j.actamat.2013.08.018](https://doi.org/10.1016/j.actamat.2013.08.018)
20. Čapek, J.; Máthis, K.; Clausen, B.; Stráská, J.; Beran, P.; Lukáš, P.; *Mater. Sci. Eng., A*, **2014**, *602*, 25.
DOI: [10.1016/j.msea.2014.02.051](https://doi.org/10.1016/j.msea.2014.02.051)
21. Zhu, S. Q.; Yan, H.G.; Liao, X.Z.; Moody, S.J.; Sha, G.; Wu, Y.Z.; Ringer, S.P.; *Acta Mater.*, **2015**, *82*, 344.
DOI: [10.1016/j.actamat.2014.09.006](https://doi.org/10.1016/j.actamat.2014.09.006)
22. Minárik, P.; Král, R.; Pešička, J.; Daniš, S.; Janeček, M.; *Mater. Charact.*, **2016**, *112*, 1.
DOI: [10.1016/j.matchar.2015.12.002](https://doi.org/10.1016/j.matchar.2015.12.002)
23. Song, Y.; Yoon, E.Y.; Lee, D.J.; Lee, J.H.; Kim, H.S.; *Mater. Sci. Eng., A*, **2011**, *528*, 4840.
DOI: [10.1016/j.msea.2011.02.020](https://doi.org/10.1016/j.msea.2011.02.020)
24. Valiev, R.Z.; Islamgaliev, R.K.; Alexandrov, I.V.; *Prog. Mater. Sci.*, **2000**, *45*, 103.
DOI: [10.1016/S0079-6425\(99\)00007-9](https://doi.org/10.1016/S0079-6425(99)00007-9)
25. Rauch, E.F.; Véron, M.; *Mater. Charact.*, **2014**, *98*, 1.
DOI: [10.1016/j.matchar.2014.08.010](https://doi.org/10.1016/j.matchar.2014.08.010)
26. Hautojärvi, P.; *Positrons in Solids*, Springer: Berlin, **1979**.
DOI: [10.1007/978-3-642-81316-0](https://doi.org/10.1007/978-3-642-81316-0)
27. Bečvář, F.; Čížek, J.; Lešták, L.; Novotný, I.; Procházka, I.; Šebesta, F.; *Nucl. Instrum. Methods Phys. Res., Sect. A*, **2000**, *443*, 557.
DOI: [10.1016/S0168-9002\(99\)01156-0](https://doi.org/10.1016/S0168-9002(99)01156-0)
28. Qiuzu, L.; Xiaofeng, D.; Yanping, L.; Xiaojia, W.; *J. Alloys Compd.*, **2017**, *690*, 961.
DOI: [10.1016/j.jallcom.2016.08.056](https://doi.org/10.1016/j.jallcom.2016.08.056)
29. Peng, Q.; Huang, Y.; Meng, J.; Li, .; Kainer, K.U.; *Intermetallics*, **2011**, *19*, 382.
DOI: [10.1016/j.intermet.2010.11.001](https://doi.org/10.1016/j.intermet.2010.11.001)
30. Huang, Z.; Yang, L.; You, S.; Gan, W.; Kainer, K.U.; Hort, N.; *J. Magnesium Alloys*, **2016**, *4*, 173.
DOI: [10.1016/j.jma.2016.08.002](https://doi.org/10.1016/j.jma.2016.08.002)
31. Vrátná, J.; Janeček, M.; Stráský, J.; Kim, H.S.; Yoon, E.Y.; *Magnesium Technology*, **2011**, 589.
DOI: [10.1007/978-3-319-48223-1_108](https://doi.org/10.1007/978-3-319-48223-1_108)
32. Vrátná, J.; Janeček, M.; Čížek, J. et al.; *J. Mater. Sci.*, **2013**, *48*, 4705.
DOI: [10.1007/s10853-013-7151-x](https://doi.org/10.1007/s10853-013-7151-x)



A Monthly Journal

Publish your article in this journal

Advanced Materials Letters is an official international journal of International Association of Advanced Materials (IAAM, www.iaamonline.org) published monthly by VBRI Press AB from Sweden. The journal is intended to provide high-quality peer-review articles in the fascinating field of materials science and technology particularly in the area of structure, synthesis and processing, characterisation, advanced-state properties and applications of materials. All published articles are indexed in various databases and are available download for free. The manuscript management system is completely electronic and has fast and fair peer-review process. The journal includes review article, research article, notes, letter to editor and short communications.

VBRI Press
Commitment to Excellence

www.vbripress.com/aml

Copyright © 2017 VBRI Press AB, Sweden